

## High-yielding and Continuous Fabrication of nano-sized explosive crystal via Electro spraying Deposition

Chuan Huang\*, Zhijian Yang

Institute of Chemical Materials, China Academy of Engineering Physics, Mianyang,  
621900, China

Tel.: + 86 816 2495175

E-mail addresses: huangchuan28@hotmail.com

**Abstract:** As a typical kind of organic small molecular materials, energetic materials have drawn increasing interests for their unique high-energy performance. And in the current field, high performance and safety explosives are always the subject of research since the discovery of explosives. One of effective way to achieve this goal is designing and fabricating energetic co-crystal, which can potentially offer the improvements of formulation density and sensitivity. The other one is to reduce crystal size of explosive. However, the flexible, continuous and high-yielding fabrication of nano-sized energetic co-crystals has been proved to be very challenging. We have successfully fabricated the nanoparticles stacked 2,6-diamino-3,5-dinitropyrazine-1-oxide (LLM-105) sub-microsphere and a series of nano-sized CL-20 based energetic co-crystals. The electro spray, thus, can offer a flexible and versatile approach for continuous and high-yielding synthesis of nano-sized crystal explosives with preferable safety performance.

### Instruction:

Energetic materials, specially involved in monomolecular nitramine materials such as 2,4,6,8,10,12-hexanitrohexaazaisowurtzitane (CL-20), hexahydro-1,3,5-trinitro-1,3,5-triazine (RDX) and 1,3,5,7-tetranitro-1,3,5,7-tetraazacyclooctane (HMX) etc., which can quickly release a large amount of stored chemical energy when actuated, are widely used in military field as explosives, propellants and pyrotechnics.<sup>1-3</sup> As one of the most powerful explosives, CL-20 is a promising substitute for the commercially used RDX and HMX (its energy is 14-20 % higher than HMX), however, its large scale application in explosive field has been limited by the part of the intrinsic high sensitivity.

Well known, one of the effective approaches to solve this problem is developing energetic co-crystals, which can offer an opportunity to produce new materials with novel properties compared with the original components. Moreover, reduction of crystal size is believed to be another feasible method to decrease the sensitivity since smaller crystals contain less amount of defects and inclusions. Over the last decade, there has been intensive research interests for the nano-energetic materials due to their preferable burning rate and energy release rate in comparison to those micro-sized energetic materials.<sup>4,5</sup> It is believed that the excellent performance of nano-energetic materials is associated with their high specific surface area. When reduced

to nanoscale, these high explosives exhibit significantly lower sensitivity to exterior stimuli in comparison to larger particles.<sup>6-10</sup> Considering that, combining co-crystallization and nanotechnology to fabricate nanoscale energetic co-crystals would be very attractive.

In this work, we report using the electrospray deposition to nanoparticles stacked 2,6-diamino-3,5-dinitropyrazine-1-oxide (LLM-105) sub-microsphere and a series of nano-sized CL-20 based energetic co-crystals.

## **2. EXPERIMENTAL SECTION**

### **2.1 Materials**

LLM-105 raw materials was offered in our institute with purity of 99%. N, N-dimethylformamide (DMF, AR grade) and N-methyl pyrrolidone (NMP, AR grade) were purchased from Chengdu United Chemical industry (Chengdu, China). CL-20 ( $\epsilon$ -phase) was provided by Liaoning Qing Yang Chemical Industry Co., Ltd of China. TNT and DNB was offered by East Chemical Industry Company. TNB was synthesized and purified in our institute. Acetone, ethyl acetate, 2-butanone and *n*-butyl acetate were purchased from Sinopharm Chemical Reagent Co., Ltd. All reagents were used as received.

### **2.2 Characterization**

The morphology information was obtained from the field emission scanning electron microscopy (FE-SEM, Sigma HD, ZEISS) operating at 5 kV. Samples were cut from aluminum foil, and mounted on aluminum stubs sputter-coated by an ultrathin layer of gold. X-ray diffraction (XRD) measurements were carried out at room temperature by an X-ray diffractometry system (D8 Discover, Bruker) using Cu- $\alpha$  radiation with a voltage of 50 kV and a current of 30 mA. Samples were scanned from 5°-60°.

Thermal properties of samples were performed on a simultaneous thermal analysis (TG/DSC1, METTLER TOLEDO). Typically, samples (2-3 mg) were placed in a 70  $\mu$ L alumina crucible and heated from room temperature to 500 °C at a constant heating rate of 10 °C/min. All tests were performed under a nitrogen atmosphere with a flow rate of 40 mL/min.

The intermolecular hydrogen bond of products was detected by a home-made terahertz (THz) spectrum, which contains a femtosecond fiber laser producing 100 fs laser pulse with a central wavelength of 1550 nm and a photoconductive antenna detector. Before testing, a certain amount of samples comprising the products and polyethylene with a 1:1 mass ratio were grinded and then pressed to form a pellet of 5 mm in diameter and approximate thickness of 1 mm. The THz spectra was recorded from 0.1 to 3.0 THz.

## **3. RESULTS AND DISCUSSION**

### **3.1 nanoparticles stacked 2,6-diamino-3,5-dinitropyrazine-1-oxide (LLM-105)**

### sub-microsphere

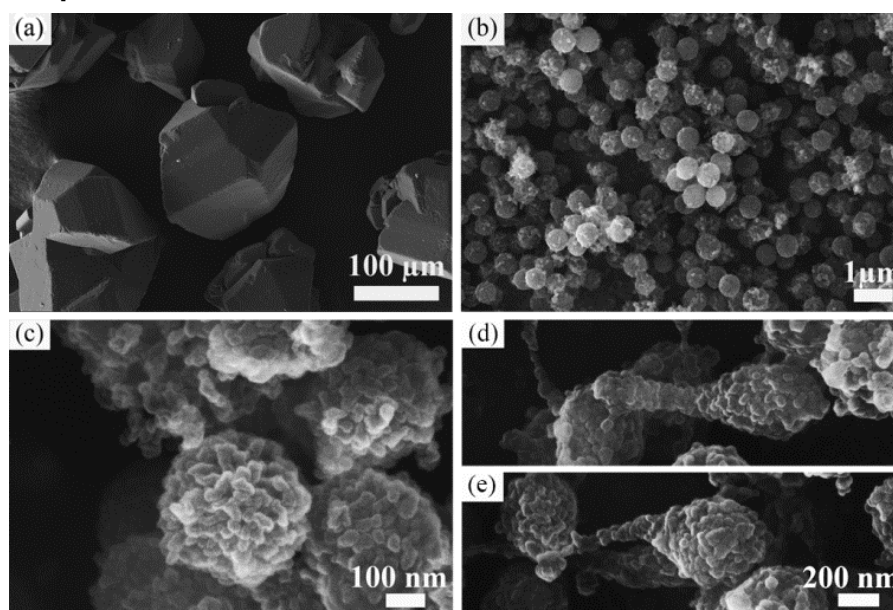


Figure 1. (a)SEM image of raw LLM-105; (b-e) SEM images of as-electrosprayed

Note: d and e have the same magnification.

The morphology of raw LLM-105 and as-electrosprayed LLM-105 particles was investigated by FE-SEM and the result is shown in Figure 1. In Figure 1a, the raw LLM-105 reveals the twin crystal with the size of about 150 $\mu$ m, and some of them have smooth crystal surface. In contrast, the morphology and size of particle electrospayed by using a flow rate of 0.05 mm/min and 27 G nozzle makes significant change. As seen in Figure 1b, these particles are sphere and monodisperse, and have size distribution from 200 – 500 nm. Additionally, some little satellite particles with diameter ranging from 40-60 nm around spheres were observed, the origins of which could be ascribed to the Coulomb fission (the detailed will be discussed in next). To further investigate the surface information of as-prepared sub-microspheres, the enlarged image of one part of Figure 1b is shown in Figure 1c. It is clearly seen that the microsphere is stacked with nanoparticles with the average diameter of  $50 \pm 10$  nm. Interestingly, besides the spheres some other shapes such as 'spindle' (Figure 1d) and 'tadpole' (Figure 1e) with the same size were obtained, while these shapes were also constituted by nano-particles. In general, nanoparticles easily form aggregates due to the inherent character of high surface energy.

For evaluation of the thermal behavior, the TG/DSC tests were performed. Figure 2a shows the TG curves of raw materials and sub-microspheres. It is apparent that there are two obvious stages in the TG curve of raw LLM-105, one started at 247  $^{\circ}$ C with a slight mass loss, the other at  $\sim$ 370  $^{\circ}$ C with a sharp weight loss, and the mass remaining at 500  $^{\circ}$ C is 2.7 %. Similarly, sub-microspheres also give two step, one beginning at 215  $^{\circ}$ C, another at  $\sim$ 350  $^{\circ}$ C, and the residue at 500  $^{\circ}$ C is 4 % which is slightly higher

than the raw materials. Clearly, the two mass loss stages of sub-microspheres are respectively smoother than the raw materials. The DSC curve of raw materials gives two exotherms (Figure 2b), a weak one where the peak temperature is at 294 °C, and a sharp one where the peak temperature is at 351 °C. The two exothermic peaks are well corresponding to the mass loss. In contrast, the DSC curve of sub-microspheres just gives one exotherm (Figure 2b) at the range of 260 – 360 °C with the peak temperature at 337 °C. The explanation of only one exotherm could be that the degradation of the slight mass loss is too mild to detect the exothermic peak. Furthermore, compared with the main exotherm of raw materials, it is clear that the peak temperature of sub-microspheres is ahead of raw materials, however, its exotherm has a lower intensity (agreement with the TG signals). The possible reason is that the sub-microspheres consisted of nano-crystals have higher surface area that causes the lower onset decomposition temperature (the similar result are also found in nano- and micro-thermits). However, the exothermic reaction of explosive is depended on the molecular structure not the particle size, nanoparticle-stacked sub-microspheres have larger bulk volume which can increase the heat loss in the degradation process, resulting in the lower intensity.

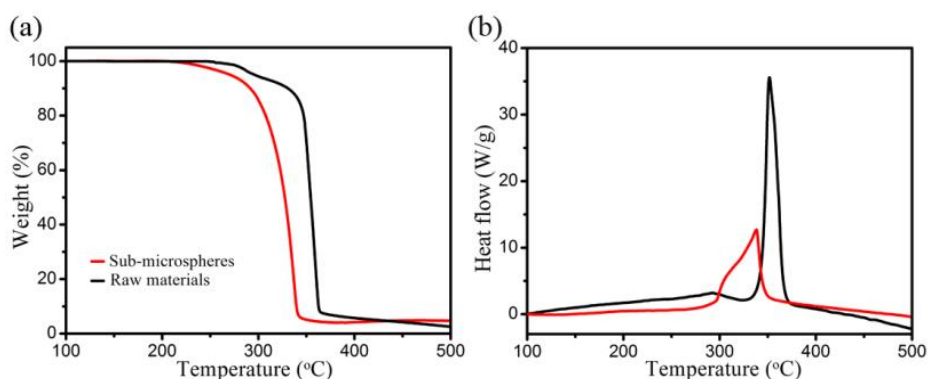
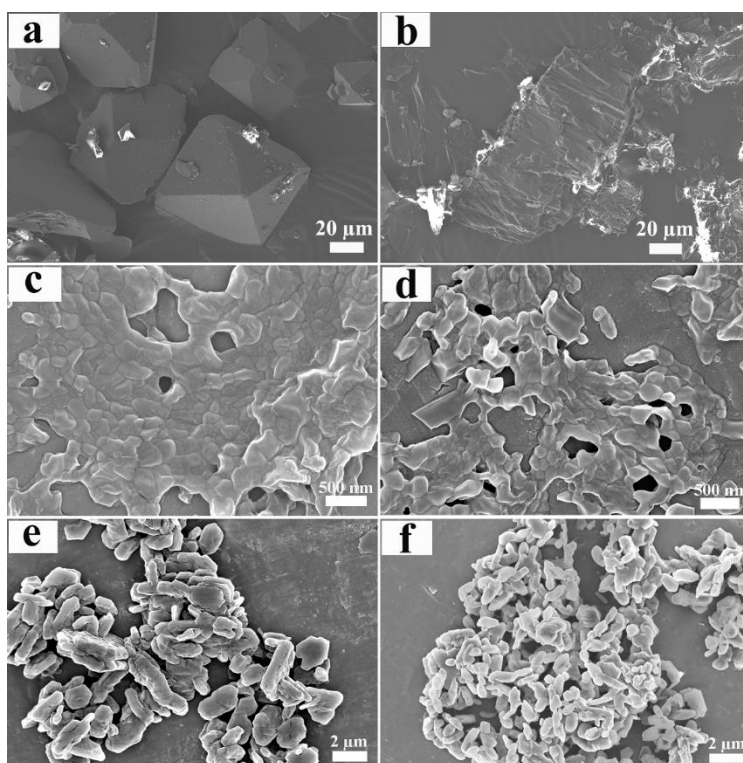


Figure 2. The thermal analysis of the raw LLM-105 and the sub-microspheres, (a) TG curves; (b) DSC curves

### 3.2 Preparation and solvent effects of CL-20/TNT nano-cocrystals

Figure 3 shows the SEM images of raw materials and CL-20/TNT co-crystal particles fabricated by electrospray from these solvents. Clearly, both of raw  $\epsilon$ -CL-20 (Figure 3a) and TNT (Figure 3b) show the high crystallinity and have a size distribution up to hundreds of micrometers. As expected, all prepared products are fine particles at nanoscale, although the used solvents have different boiling points (ranging from 56 °C to 126 °C) which have a significant effect on the evaporation rate of electrosprayed droplets. Among these products, particles fabricated from acetone (Figure 3c) and 2-butanone (Figure 3d) have similar morphology and size distribution ranges around 200 nm. While, those CL-20/TNT co-crystal particles prepared from ethyl acetate (Figure 3e) and *n*-butyl acetate (Figure 3f) present a quite different morphology and greater

size distribution (1 $\mu$ m to 2 $\mu$ m) in comparison to those from ketone solvents. It is believed that crystal nucleation and growth are mainly influenced by the solvent-solute interaction, solubility, rate of supersaturation and the volatility of solvent. Since the time of flight of droplets in electrospray process is very short, the rate of supersaturation will not play a key role on the effect of crystal morphology. In general, high solvent volatility is beneficial for rapid and massive nucleation, resulting fine particles, while low solvent volatility corresponds to large crystal size. In addition, high solubility also prefers the small particles. In our case, the used ketone solvents have the high volatility and high solubility for CL-20 and TNT in comparison to ester solvents, well corresponding to the observed SEM results. However, for results obtained from ethyl acetate and *n*-butyl acetate, we believe that the solvent-solute has predominant effect on the crystal size since ethyl acetate has the higher volatility and solubility but obtains the larger crystal size comparing to *n*-butyl acetate. Generally, the solvent-solute interaction involves van der Waals and hydrogen bonding. The strength of solvent-solute van der Waals interaction can be mainly evaluated by the dipolar polarizability and the strength of hydrogen bonding can be evaluated by the hydrogen bond donor ability. According to the reported, the value of hydrogen bond donor of ethyl acetate and *n*-butyl acetate are both zero, and the dipolar polarizability of ethyl acetate and *n*-butyl acetate are 55 and 46 respectively, indicating the van der Waals interaction can be the key solvent-solute interaction in our experiments.



**Figure 3** SEM images of raw materials (a)  $\epsilon$ -CL-20, (b) TNT, and electrospayed CL-20/TNT co-crystal particles from: (c) acetone, (d) 2-butanone, (e) ethyl acetate, (f) *n*-

butyl acetate.

The PXRD patterns of the electrosprayed CL-20-TNT products from different solvents and raw materials are illustrated in Figure 4 together with the calculated PXRD patterns for CL-20-TNT co-crystal. The similar trend is observed in all PXRD patterns of CL-20-TNT products. In these patterns, the presence of TNT can be distinguished particularly from the diffraction peaks at  $8.9^\circ$ ,  $17.7^\circ$  and  $25.1^\circ$  of  $2\theta$ , which are the typical of TNT. Additionally, the typical diffraction peaks of co-crystal at  $9.8^\circ$ ,  $12.5^\circ$ ,  $14.3^\circ$  and  $21.6^\circ$  are present in all products, indicating the formation of co-crystal phase in all products. These suggest electrosprayed CL-20-TNT from these four solvents can just partially from the co-crystal, which is accordance with the result from the reference. As reported reference, rapid crystallization as SFE process can cause a structure distortion involving the interaction between CL-20 and TNT molecules and those between the adjacent CL-20 molecules, resulting in the partial formation of co-crystal. Surprisingly, the  $\epsilon$ -CL-20 is not detected, instead,  $\beta$ -CL-20 (typical diffraction peaks at  $13.7^\circ$ ,  $24.1^\circ$  and  $28.2^\circ$ ) appears in all products. To probe the formation of  $\beta$ -CL-20, we carried out the electrospray process of  $\epsilon$ -CL-20 using acetone and ethyl acetate as the solvent. The result shows that the products are  $\beta$ -CL-20 and almost no  $\epsilon$ -CL-20. In fact, CL-20 initially prefers  $\beta$ -form when crystallizing in most highly supersaturated solution since the  $\beta$ -form has the lowest lattice energy in all polymorphs, followingly, the  $\beta$ -form transforms to  $\epsilon$ -form. In our experiments, the electrospray process is transient and crystallization is depended on the rapid evaporation of solvent, directly obtaining the  $\beta$ -CL-20 and no more time transforming to  $\epsilon$ -CL-20.

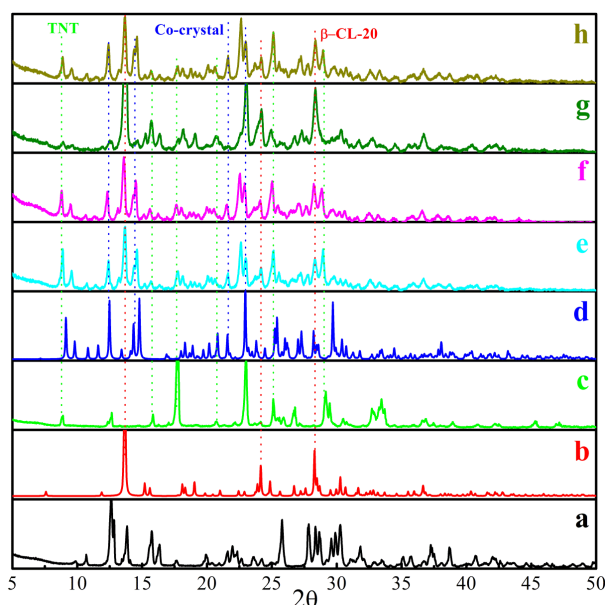


**Figure 4** PXRD patterns of raw-CL-20 (a),  $\beta$ -CL-20 (b), raw TNT (c), calculated CL-20/TNT co-crystal (d), electrosprayed CL-20/TNT co-crystal from acetone (e), ethyl acetate (f), 2-butanone (g) and in *n*-butyl acetate (h). The calculated CL-20/TNT co-

crystal PXRD patterns from the CIF.

### 3.3 Preparation and characterization of CL-20/DNB nano-cocrystals

Besides the CL-20/TNT co-crystal, we have also fabricated the CL-20/DNB products by the electrospray deposition. Figure 5b exhibits the SEM image of as-prepared CL-20/DNB co-crystal products. It is clear that the size of these products ranges from 100 to 500 nm, while the size of raw DNB (Figure 5a) and  $\epsilon$ -CL-20 (Figure 3a) is around 100  $\mu\text{m}$ . To discriminate the crystal phase of electrosprayed products, the collected samples were analyzed by PXRD. As shown in Figure 6, the PXRD pattern of electrosprayed CL-20/DNB products presents the significant difference with raw materials and  $\beta$ -CL-20, and extremely coincides the calculated pattern of CL-20/DNB co-crystal (peaks at  $5.3^\circ$ ,  $10.5^\circ$ ,  $11.7^\circ$ ,  $13.9^\circ$ ,  $17^\circ$ ,  $25.5^\circ$ ,  $26.6^\circ$ ,  $28.6^\circ$ ), indicating the formation of co-crystal phase.

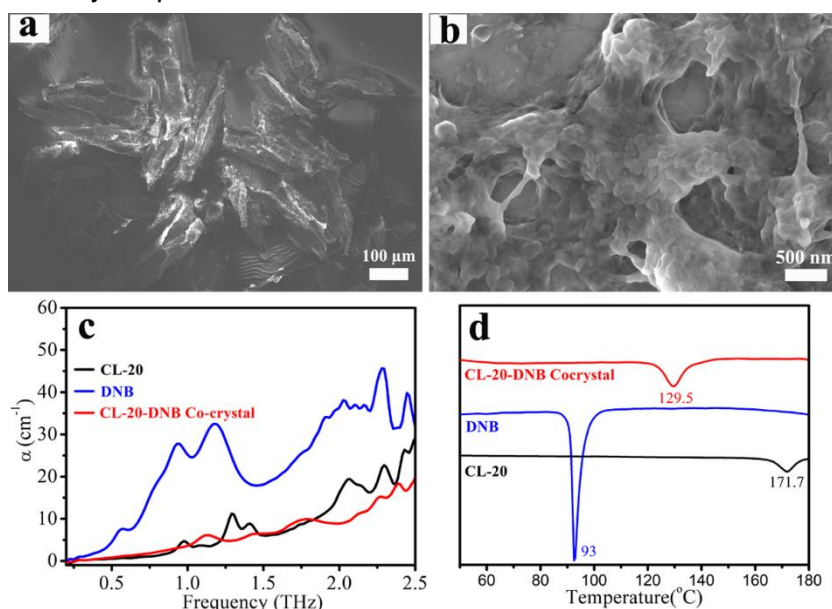


**Figure 5** SEM image of DNB (a), SEM image of electrosprayed CL-20/DNB products from acetone (b), Terahertz spectra of electrosprayed CL-20/DNB co-crystal (c), DSC curves of electrosprayed CL-20/DNB co-crystal and raw materials (d).

To probe the intermolecular reactions in the electrosprayed CL-20/DNB products, THz spectroscopy was employed to analyze the spectra of CL-20, DNB and as-prepared CL-20/DNB products, respectively. The resulted spectra presents that the as-prepared CL-20/DNB product exhibits some distinctive peaks at 1.22 and 1.77 THz (Figure 5c), where both CL-20 and DNB have negligible peaks, verifying the formation of intermolecular hydrogen bonds between CL-20 and DNB.

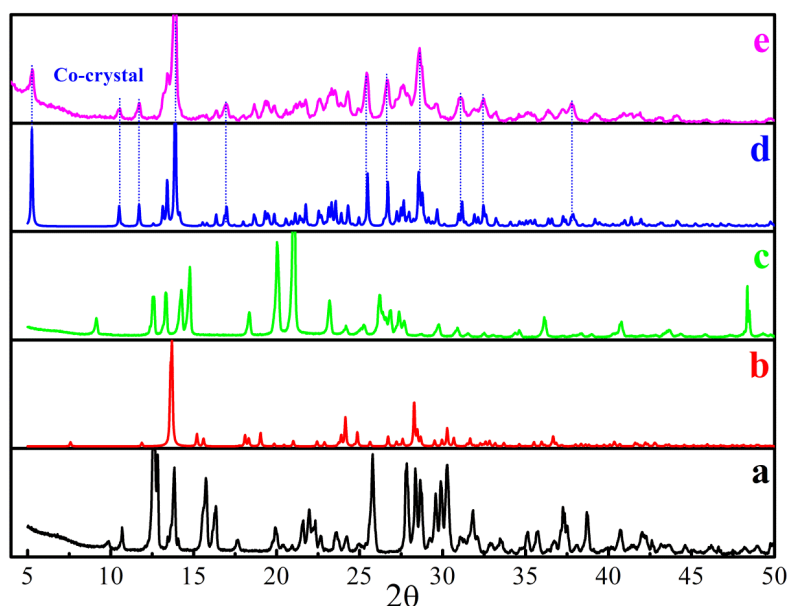


**Figure 6** PXRD patterns of raw CL-20 (a),  $\beta$ -CL-20 (b), raw DNB (c), calculated CL-20/DNB co-crystal (d), electrospayed CL-20/DNB co-crystal from acetone (e). The calculated CL-20/DNB co-crystal PXRD patterns from the CIF

Additionally, the DSC curve of as-prepared products is also distinct from the raw materials (Figure 5d). More specifically, only one endothermic peak of electrospayed CL-20/DNB is observed at 129.5 °C, significantly higher than the melting temperature of DNB (93 °C) and lower than the phase transition temperature of  $\epsilon$ -CL-20 (171.7 °C). This further proves the formation of CL-20/DNB co-crystal pure phase by such electrospaying method.

### 3.5 A novel nano-sized co-crystal of CL-20/TNB

Similarly, we have utilized electrospay method to prepare the CL-20/TNB products. SEM analysis shows the size of these products ranges from 200 to 600 nm (Figure 7b), while raw TNB shows flake shape with tens of micrometer (Figure 7a). The formation of co-crystal structure of electrospayed CL-20/TNB products could be confirmed by the inspection of PXRD patterns. From Figure 6c, the PXRD pattern of electrospayed products shows a significant difference to raw materials, including the presence of new intensive peaks at 8.5°, 10.7°, 14.5° and 22° and absence of most intensive peaks for TNB at 23° and for  $\epsilon$ -CL-20 at 12.7°, verifying the formation of new crystalline phase. To our best knowledge, the CL-20/TNB co-crystal has never been reported. It is to be regretted that the single crystal structure of this novel energetic co-crystal cannot be obtained since current characterizations are unavailable to analyze such fine product in nanoscale, nevertheless, PXRD combined with DSC and FT-IR results can confirm the formation of CL-20/TNB co-crystal. Notably, thermal analysis of electrospayed CL-20/TNB products shows an endothermic peak at 138.5 °C (Figure 6d), losing a melting endotherm of TNB (at 124.5 °C) and a phase transition endotherm



of  $\epsilon$ -CL-20 (at 171.7 °C). This complements well the PXRD data, suggesting the formation of co-crystal between CL-20 and TNB.

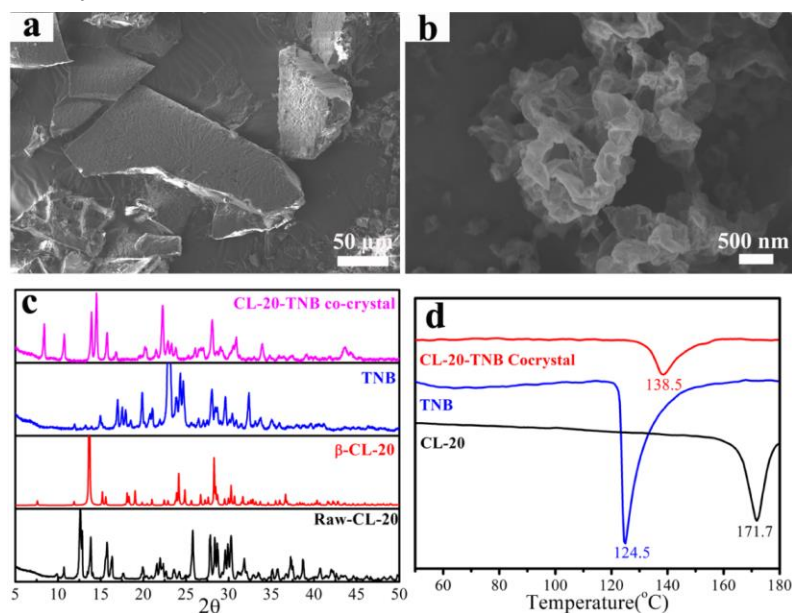


**Figure 7** SEM image of TNB (a), SEM image of electrospayed CL-20/TNB products from acetone (b), PXRD pattern of electrospayed CL-20/TNB co-crystal and raw materials (c), DSC curves of electrospayed CL-20/TNB co-crystal and raw materials (d).

#### 4. CONCLUSION

In summary, we have demonstrated using the electrospray deposition to fabricate the monodisperse LLM-105 sub-microspheres and a series of nano-sized CL-20 based energetic co-crystals. Characterization of LLM-105 sub-microspheres indicates these sub-microspheres ranging from 200 to 500 nm were consisted of the 50 nm nanoparticles, even though preserved six months these sub-microspheres also had the same morphology. The size of CL-20 based co-crystal has ranged from 200-600 nm. And several of characterizations have confirmed the partial formation of CL-20/TNT co-crystals, all CL-20/DNB cocrystal and new CL-20/TNB co-crystals. This facile technique is versatile and could be extended to the preparation of other nanoparticle-stacked sub-microsphere explosives and provide an efficient screening to quickly distinguish whether two energetic materials can form co-crystal.

#### References

- (1) Sikde, A. K.; Sikder, N. J. Hazard. Mater. 2004, 112, 1-15.
- (2) Thottempudi, V.; Shreeve, J. M. J. Am. Chem. Soc. 2011, 133, 19982-19992.
- (3) Severac, F.; Alphonse, P.; Esteve, A.; Bancaud, A.; Rossi, C. Adv. Funct. Mater. 2012, 22, 323-329.
- (4) Ostmark, H.; Bergman, H.; Sjöberg, P. Proc. Energ. Mater. Technology, Phoenix, 1995, pp. 75-81.

- (5) Sider, A. K.; Sikder, N.; Gandhe, B. R.; Agrawal, J. P.; Singh, H. Defence. Sci. J. 2002, 52, 135-146.
- (6) Zhang, J. CrystEngComm, 2016, 18, 6124-6133.
- (7) Bolton, O.; Simke, L. R.; Pagoria, P. F.; Matzger, A. J. Cryst. Growth Des. 2012, 12, 4311-4314.
- (8) Aakeröy, C. B.; Wijethunga, T. K.; Desper, J. Chem.-Eur. J. 2015, 21, 11029-11037.
- (9) Pessina, F.; Schnell, F.; Spitzer, D. Chem. Eng. J. 2016 , 291, 12-19.
- (10) Jung, W.; Park, J.; Lee, W.; Lee, J.; Koo, K.; Oh, M. Chem. Eng. Technol. 2016, 39, 1309-1316.
- (11) Lee, J. E.; Kim, J. W.; Han, S. K.; Chae, J. S.; Lee, K. D.; Koo, K. K. Ind. Eng. Chem. Res. 2014, 53, 4739-4747.